LANGMUIR

pubs.acs.org/Langmuir
Article

Wetting Behavior of Inkjet-Printed Electronic Inks on Patterned Substrates

Pooja Arya,*,# Yanchen Wu,# Fei Wang,* Zhenwu Wang, Gabriel Cadilha Marques, Pavel A. Levkin, Britta Nestler, and Jasmin Aghassi-Hagmann

Cite This: https://doi.org/10.1021/acs.langmuir.3c03297
Read Online

ABSTRACT: In inkjet printing technology, one important factor influencing the printing quality and reliability of printed films is the interaction of the jetted ink with the substrate surface. This short-range interaction determines the wettability and the adhesion of the ink to the solid surface and is hence responsible for the final shape of the deposited ink. Here, we investigate wetting morphologies of inkjet-printed inks on patterned substrates by carefully designed experimental test structures and simulations. The contact angles, the surface properties, and drop shapes, as well as their influence on the device variability, are experimentally and theoretically analyzed. For the simulations, we employ the phase-field method, which is based on the free energy minimization of the two-phase system with the given wetting boundary conditions. Through a systematic investigation of printed drops on patterned substrates consisting of hydrophilic and hydrophobic areas, we report that the printed morphology is related not only to the designed layout and the drop volume but also to the printing strategy and the wettability. Furthermore, we show how one can modify the intrinsic wettability of the patterned substrates to enhance the printing quality and reliability. Based on the present findings, we cast light on the improvement of the fabrication quality of thin film transistors.

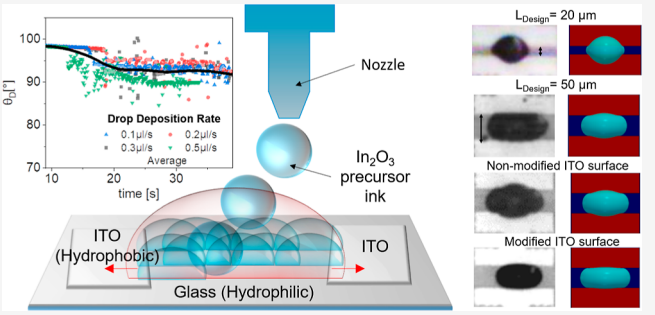

INTRODUCTION

Inkjet printing of functional inks is a promising technology to fabricate active and passive electronic devices such as RFID tags,[1] antennas,[2] transistors,[3,4] and memristors[5] for emerging electronic applications such as wearables, soft robotics, and point of care medical devices.[6,7] Moreover, this "drop on demand" (DOD) technique is compatible with diverse surfaces and substrates ranging from rigid to flexible, two-dimensional (2-D) to three-dimensional (3-D) objects. In addition, DOD inkjet technology can be utilized for a large range of materials which is locally deposited.[8−10] In accordance with the high demand of functional inks and diverse requirements of their pre- and postprinting treatment, it is important to understand the fundamentals of the inkjet printing process. The printed geometries depend upon many parameters in different printing phases, starting from optimizing the electrical/thermal conditions in the printhead to the ejection of droplets from the nozzle, to droplet deposition and droplet coalescence on the surface, and finally the drying/annealing process of the printed film.[11]

There have been thorough investigations on controlling the printing parameters, such as ink volume, nozzle voltage, waveform, flow and acoustics inside the printhead, velocity and volume of the ejected droplets, and the effect of wettability and surface tensions on the droplet formation.[12−16] Among the aforementioned factors, the wettability and surface tension of the ink are crucial for ejecting consistent droplets of desired size, shape, and volume. Different numerical models were applied to address such problems. For instance, Hu et al. used volume of the fluid method and concentrated on droplet coalescence and its effect on printing quality.[17] The friction effect was included to address contact angle hysteresis in this study. Soltman et al. have demonstrated a method to optimize the inkjet printing of two-dimensional, partially wetting films.[18] Seemann et al. investigated the equilibrium morphology of a drop on mechanically structured surfaces that suffers from the pinning effect of the contact line. This pinning effect is caused by the variation of the local normal vector of the surface.[19] Matsui et al. numerically studied the droplet wetting on chemically patterned substrate via surface evolver within the context of the sharp interface model.[20] In these studies, only Young's contact angle is employed to ascertain the macroscopic contact angle. Other contact angles, including

Received: October 30, 2023
Revised: December 22, 2023
Accepted: January 18, 2024

advancing, receding, and dynamic contact angles, which are closely tied to surface structure and dynamics, are not taken into consideration.

To control and manipulate the wetting behavior of droplets on the substrate, diverse methods for fabricating chemically patterned surfaces have been reported in the last decades. Various techniques including transfer printing,[21] microcontact printing,[22] soft lithography,[23,24] and inkjet printing[25,26] have been used to fabricate a chemically patterned surface with hydrophobic and hydrophilic wettability contrast. Zheng et al.[21] utilized the transfer printing technique and PDMS-based stamps to functionalize the substrates to generate hydrophilic and hydrophobic patterns, which is a contact approach for printing and requires high processing temperatures. Benor et al.[22] demonstrated the microcontact printing technique, which is a continuous drop deposition method. Lee et al.[23] developed a simple and low-cost surface wettability patterning based on soft lithography processes to control the printing variation. Sung et al.[24] combined inkjet printing with soft lithography and produced a surface wettability contrast up to 104°. Park et al.[26] systematically investigated the influence of ink viscosity, deposition speed, solvent polarity, and boiling point and obtained high resolution and fine pitch printed silver nanoparticulate electrodes. Nishimoto et al.[25] have shown an interesting approach to make hydrophobic and hydrophilic patterns using inkjet printing technology. In this study, we create a hydrophobic−hydrophilic pattern through laser ablation of indium tin oxide (ITO)-coated glass and modify the ITO surface using a chemical deposition technique. The final printing results are directed by the systematic coalescence of multiple small droplets. The present method is a completely noncontact approach for printing and does not require high processing temperatures. Differing from the mechanically patterned surface, on which the pinning effect is caused by the variation of the local normal vector of the surface, the wettability contrast on a chemically patterned surface leads to the pining of the contact line due to the inhomogeneous wall energy.

Although the wetting behavior of a drop on homogeneous and heterogeneous surfaces has been largely studied in the last few decades both experimentally and through simulations, there are still challenges to completely understand the wetting phenomenon, as it is highly related to different factors, such as the drop deposition method, surface energies, dynamics, etc. In particular, the measurement of the real contact angle on a heterogeneous surface remains an unresolved issue. On real patterned substrates, the pinning effect of the roughness and chemical patterns gives rise to the contact angle hysteresis,[27−31] so that the contact angle is in a range bounded by the advancing and receding contact angles, which can be measured by the inflation and deflation of the drop. The randomly distributed surface defects result in high device-to-device variation, leading to a major problem, specially in the applications requiring a high level of precision, as in the case of arrays of logic gates, sensors, digital circuits, etc.[32]

In this work, we focus on the fabrication of indium oxide-based semiconductor films using DOD inkjet printing technology with the goal to print electrolyte-gated thin film transistors (TFT).[33,34] It has been reported that the performance (threshold voltage: V_{th}, on current: I_{on}, and off current: I_{off}) of the transistor device is highly dependent on its width-by-length ratio, which is directly related to the dimensions of the printed semiconductor layer.[4] For this reason, our objective is to thoroughly investigate the printing process for the semiconductor layer. In the case of top gated transistors (Figure S2), the semiconductor layer is printed on a hydrophilic glass surface between two electrodes, which are intrinsically hydrophobic in material (ITO). Therefore, it is of vital importance to understand the wetting behaviors of the printed ink on a real patterned surface.

Specifically, we consider a real substrate consisting of surface roughness (mechanical heterogeneity) and chemical heterogeneity. We investigate the equilibrium drop morphologies for different printing parameters, like drop volume (100, 200, ···, 1200 pL), surface wettability, and printing strategies (one-dimensional printing or two-dimensional printing). The 1-D and 2-D printing style affects the final shape of the printed drop because of the pinning effect on the comparatively rougher glass surface, as it results in multiple metastable states. The process of drop deposition is very dynamic, and the printed film is formed from a systematic coalescence of multiple small droplets. By considering this dynamic process and the roughness of the surface, we choose reasonable contact angles on the real surfaces to have a better prediction of drop shapes on patterned surfaces, which has not been extensively explored in the context of inkjet printing. These important contact angles include dynamic and thermodynamic contact angles. The dynamic contact angle is closely related to the printing strategy and will be determined via mimicking the printing dynamics in the measurement of the contact angle with a low Weber number. The thermodynamic contact angle is theoretically determined through advancing and receding contact angles, both of which are directly measured in experiments. The shape, i.e., the printed width, length, and total base area of the final drop (which is the combination of the previously printed multiple droplets) with respect to printing parameters and the total volume of the drop are systematically studied. Phase-field (PF) simulations are accordingly conducted to confirm the experimental results within the context of the diffuse interface approach. The diffuse interface model contains a low-order derivative of the order parameter and is more numerically efficient than the sharp interface model. The PF model has already been proven to be a reliable and robust approach for simulating the static wetting morphology of droplets on solid substrates. In the PF model, input parameters such as contact angles are measured on both the ITO surface and the rough glass surface through experiments. We reduce the fabrication variability of printed field effect transistors to enhance the device performance by chemically functionalizing the ITO surface through silanization and the thiol−ene photoclick patterning process. From a technological point of view, our strategy provides guidelines to improve the fabrication quality and guarantee the low contact resistance of the device. In addition, our findings can be a useful predictive method to generate an optimized physical layout of large-scale electronic devices. At last, we show possible outcomes for high throughput transistor fabrications with minimum device-to-device variations, which requires a controlled printing system on patterned surfaces with the method proposed in the present work.

EXPERIMENTS AND MODELING

Experimental Setup. Commercially available ITO-coated glass slides of dimensions 20 × 20 mm and thickness 1.1 mm (from Präzisions Glas & Optik GmbH) are used as substrates. The laser ablation technique is deployed to structure the ITO-coated glass in

https://doi.org/10.1021/acs.langmuir.3c03297
Langmuir XXXX, XXX, XXX−XXX

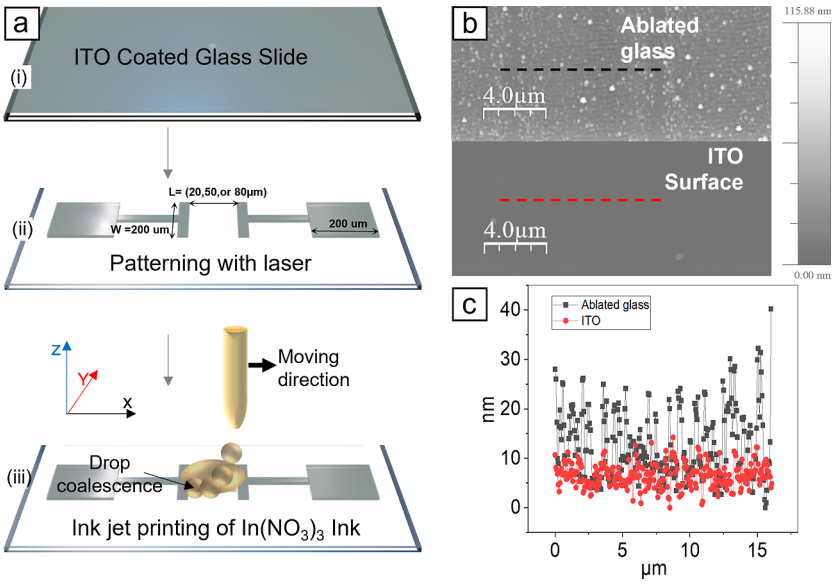

Figure 1. (a) Scheme of the fabrication process of the semiconductor film on patterned substrates: structuring of the ITO-coated glass via the laser ablation technique and the drop-on-demand ink jet printing of indium nitrate precursor ink. (b) AFM images of the ablated glass and ITO surface (see the corresponding SEM images in Figure S3). (c) Height profile of the ablated glass and ITO surface. The maximum height of the roughness on glass and ITO surfaces is 30 and 10 nm, respectively.

order to use ITO coating directly as source and drain electrodes, as shown in Figure 1a. The semiconductor film is based on a self-made indium nitrate precursor ink with the following physical properties, density ρ: 1.032 g/cm^3, surface tension γ_{lg}: 57.6 mN/m, and viscosity μ: 1.5 mPa s. The film is printed between the electrodes using a DOD inkjet printer (DMP-2800 FUJIFILM, Inc.). The printed film is further annealed at 400 °C for 2 h to obtain an indium oxide film.

The printer consists of a disposable ink cartridge and a print-head with 16 nozzles, where each nozzle can eject a single ink droplet of 10 pL. In this work, only one nozzle is used for printing. Other parameters including the droplet spacing (center to center distance between two consecutive drops, e.g., d = 10 μm), frequency (5 kHz), print-head distance from the stage (1500 μm), and an adequate waveform to print 10 pL drop are kept constant throughout the fabrication process. The printing is performed at room temperature. Optical images of final drops are captured using a preinstalled optical camera within the printer. Surface parameters (area, width, and length) of printed drops are calculated for physically equilibrated drops. Time-dependent video of inkjet deposited 300 pL drop is shown in Supporting Information to confirm that there is almost no change in the base area with time.

To modify the surface properties, and hence wetting behavior, the chemical functional group is used to modify ITO glass slides through the silanization with trichlorovinylsilane and thiol−ene photoclick patterning processes.[35] The modified ITO surface is then patterned through laser ablation to use the ITO-coated structure directly as electrodes. Contact angles of ink on the modified ITO, nonmodified ITO, and laser-ablated glass surfaces are measured using a contact angle setup from DataPhysics Instrument GmbH. Printed areas, widths, and lengths are acquired using measurement plugin tool in ImageJ (Rasband, W. S., ImageJ, U.S. NIH, Bethesda, MD, USA).

Numerical Model. For the numerical model, we adopt a volume-preserved Allen−Cahn-type PF model,[36] which is implemented within the in-house code "Parallel Algorithms for Crystal Evolution in 3D" (PACE3D).[37] We apply this model to simulate the equilibrium shapes of drops on the patterned surfaces, where contact angles on different areas from experiments are used to set up the modeling parameters in the simulations. This model has been fully validated for simulating the drop morphology on homogeneous surfaces[38] and chemically patterned substrates.[39] Herein, we give a concise description of this method and refer to refs 38 and 40 for the details. We introduce a space- and time-dependent order parameter $\phi(\boldsymbol{x}, t)$ to describe the phase states. The parameter $\phi(\boldsymbol{x}, t)$ changes promptly but continuously from 0 to 1 across the liquid−gas interface. In the bulk phases, we have $\phi = 1$ and $\phi = 0$, corresponding to liquid (l) and gas (g) phases, respectively. Specifically, the liquid and gas phases described here correspond to ink and air in experiments. The free energy functional of the system reads

$$\mathcal{F} = \int_\Omega [(1/\epsilon)w(\phi) + f_0(\phi) + \epsilon\gamma_{lg}(\nabla\phi)^2]\mathrm{d}\Omega + \int_S f_w(\phi)\mathrm{d}S \tag{1}$$

where Ω is the spatial domain, ϵ indicates the width of the liquid−gas interface, and S represents the solid−liquid boundary. The obstacle potential $w(\phi)$, which provides a cutoff or obstacle against nonphysical values of ϕ,[41] is given as $w(\phi) = (16/\pi^2)\gamma_{lg}\phi(1-\phi)$, if $0 \le \phi \le 1$; and $w(\phi) = +\infty$, if $\phi < 0$ or $\phi > 1$. The bulk free energy density $f_0(\phi)$ contributes to the volume preservation[36] and $\epsilon\gamma_{lg}(\nabla\phi)^2$ denotes a gradient energy density. The wall free energy density f_w is formulated as

$$f_w(\phi) = \gamma_{ls}h(\phi) + \gamma_{gs}[1 - h(\phi)] \tag{2}$$

Here, $h(\phi) = \phi^3(6\phi^2 - 15\phi + 10)$ is an interpolation function. γ_{ls} and γ_{gs} are, respectively, the interfacial tensions of the liquid−solid and gas−solid interfaces. By minimizing the free energy functional via the variational approach, we obtain

$$\tau\epsilon\partial_t\phi = -(16/\pi^2)\gamma_{lg}(1-2\phi)/\epsilon + 2\epsilon\gamma_{lg}\Delta\phi - f_0'(\phi) \tag{3}$$

where τ is a time relaxation coefficient, which accounts for the relaxation toward equilibrium state. The natural boundary condition corresponding to a local equilibrium at the wall[42,43] is utilized in the present model, which is given as

$$2\epsilon\gamma_{lg}\nabla\phi\cdot\boldsymbol{n} + f_w'(\phi) = 0 \tag{4}$$

Here, $\boldsymbol{n}$ is a pointing-out normal vector of the solid−liquid boundary. This boundary condition is consistent with Young's law.[44]

In the simulations, the relevant variables are nondimensionalized by the characteristic length x^*, characteristic time t^*, and characteristic surface tension σ^*, respectively. The values for these characteristic variables are listed in Table S1, and the related modeling parameters are comprehensively discussed in Section 1 of Supporting Information. The parameters γ_{ls} and γ_{gs} are chosen according to the corresponding contact angles from experiments based on Young's law.

https://doi.org/10.1021/acs.langmuir.3c03297
Langmuir XXXX, XXX, XXX−XXX

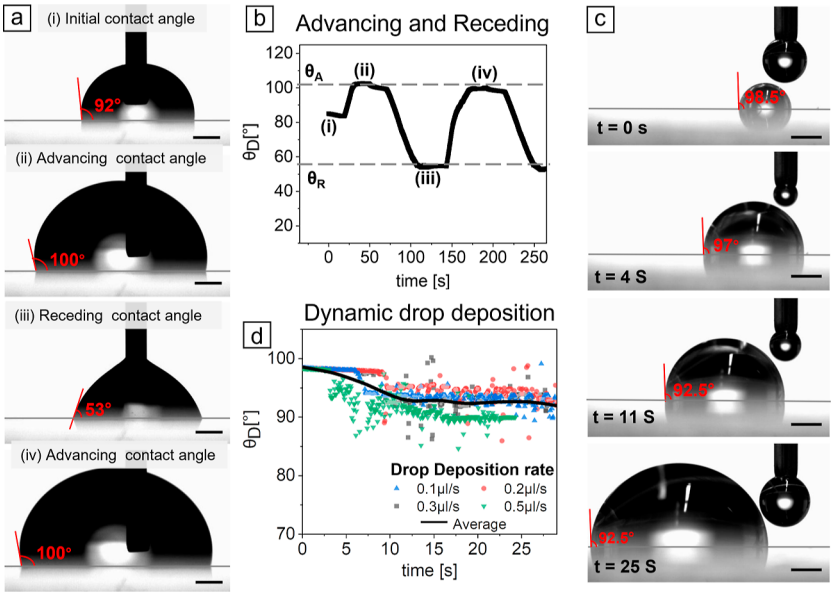

Figure 2. Optical micrograph of indium nitrate precursor ink drop on the ITO-coated surface. (a) Advancing and receding contact angles by the needle-in method. (i) Initial drop, (ii) advancing contact angle θ_A, (iii) receding contact angle θ_R, and (iv) θ_A. (b) Dynamic contact angle θ_D is plotted against increasing (reaching θ_A) and decreasing (toward θ_R) volume of the ink with time. The advancing contact angle θ_A and receding contact angle θ_R on the ITO surface are measured as 100 and 53°, respectively. (c) Contact angle based on dynamic drop deposition with a drop volume flow rate of 0.5 μL/s is measured for the ITO surface on a moving stage. (d) Dynamic contact angle θ_D is plotted with time for different drop deposition rates. The average contact angle for dynamic droplet deposition is measured as 92.5°, as guided by the black solid line and used for the numerical simulation. Scale bars: 0.5 mm. The corresponding videos for (a–c) are included in Supporting Information Section.

By solving eqs 3 and 4, the equilibrium shapes of drops can be obtained, which are used to compare with experimental results.

RESULTS AND DISCUSSION

Contact Angles of Printed Indium Nitrate Precursor Ink on ITO and Ablated Glass Surface. DOD inkjet printing is a dynamic process. Namely, multiple droplets each of 10 pL are printed and then fused together to form an ink film with a larger volume. The individual droplets can be placed either exactly on top of the previously printed droplet or with a certain drop spacing. Typically the printer is operated in the later case with a printing direction left to right along the horizontal *X*-axis. When the printed multiple droplets coalesce, a larger drop with a larger contact area to the substrate is formed. We print the ink droplets on a patterned substrate, as shown in Figure 1a bottom image. The final shape of the printed drop depends on the contact angles with both the ITO and glass substrates and the total volume of the drops.

In simulations, we define suitable contact angles on the patterned substrates, as discussed in the following. In reality, the contact angle could be any value between the advancing and receding contact angles. Therefore, it is wise to choose a proper contact angle according to the patterns on the substrate and the printing process. The advancing contact angle θ_A and receding contact angle θ_R for the ITO surface are measured with the so-called "needle-in-the-sessile drop method",[45] as shown in Figure 2ai–iv. The measured contact angle as a function of time is plotted in Figure 2b, where θ_A = 100° and θ_R = 53° are obtained for the ITO surface. Using the same method, the advancing and receding contact angles θ_A and θ_R for the modified ITO surface and the ablated glass surface are also measured and presented in Table 1. The measurement of θ_A, θ_R, and θ_D on the ablated glass surface is presented in Figure S4c,d in the Supporting Information.

Table 1. Contact Angles on Different Surfaces

surfaces	θ_A [°]	θ_R [°]	θ_{th} [°] (calculated[46])	θ_D [°]
modified ITO	115	70	87.79	110
ITO	100	53	73.18	92.5
ablated glass	89	35	59.4	

To comply with the inkjet printing process, which is used in device fabrication, the dynamic contact angle θ_D with respect to the moving ITO substrate is also measured. In this case, we first deposit a sessile drop of the ink on the ITO surface. Then we add the ink droplets through the capillary with a constant rate of Ra = 0.1, 0.2, 0.3, and 0.5 μL/s. The stage is moved horizontally such that the subsequent droplet falls partially on the previous droplet similar to the inkjet printing process. Optical images of the measurement process at different times are shown in Figure 2c. In such a dynamic process, we observe that after a few seconds of transient time, the contact angle reaches a saturation value of 92.5° on the ITO surface (see Figure 2d). This saturated contact angle is in between the advancing and receding contact angle regime but more toward the advancing angle because the contact line of the drop moves outward. On the contrary, if the stage does not move while adding liquid to the drop on the ITO surface, the contact angle reaches the advancing contact angle eventually (see Figure S4a,b in the Supporting Information). The difference between these two contact angles is caused by the different pinning force. In the situation of a dynamic process, the pinning force on the substrate is partially compensated by the inertial force of the moving droplets; thus, the dynamic contact angle θ_D is slightly smaller than the advancing contact angle θ_A. Following the same strategy, we also measure the dynamic contact angles on the modified ITO surfaces. The dynamic contact angles θ_D on the ITO and modified ITO surfaces are used as input parameters for the contact angles on the hydrophobic patterns

https://doi.org/10.1021/acs.langmuir.3c03297
Langmuir XXXX, XXX, XXX−XXX

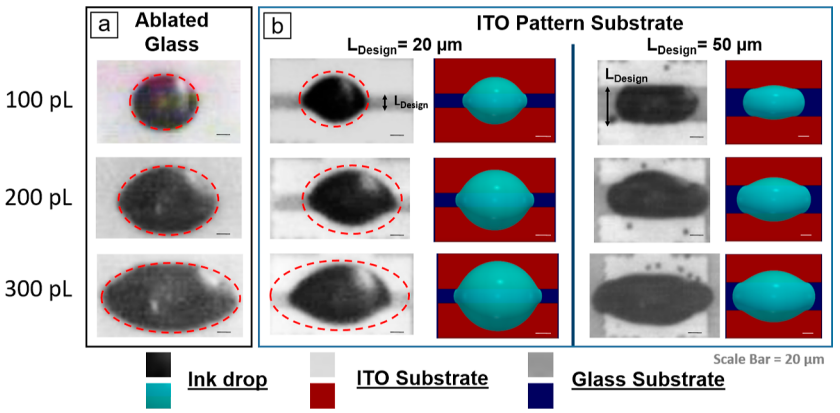

Figure 3. Optical images of inkjet-printed indium precursor ink drops of different volumes (a) on laser ablated glass; (b) between two ITO electrodes with a glass channel of L_{Design} = 20 μm and L_{Design} = 50 μm. Corresponding simulation results are shown on the right. Scale bar: 20 μm. The total volumes of 100, 200, and 300 pL are achieved by the combination of multiple equi-sized droplets, each of volume 10 pL.

in the simulations. On the ablated glass, the contact line moving tendency is dependent on the positions and drop spacing of the printed multiple droplets due to the rough surface (roughness height = 30 nm; see Figure 1b for the AFM images of the ablated glass and ITO surfaces). Here, we adopt the thermodynamic contact angle θ_{th} as the input parameter for the contact angle on the hydrophilic patterns in the simulations. The thermodynamic contact angle θ_{th} is calculated from θ_A and θ_R as theoretically proposed by Tadmor[46] and experimentally confirmed by Chibowski et al.[47] The thermodynamic contact angle θ_{th} is expressed as follows

$$\theta_{th} = \arccos\left(\frac{r_A \cos\theta_A + r_R \cos\theta_R}{r_A + r_R}\right) \quad (5)$$

where

$$r_A = \left(\frac{\sin^3\theta_A}{2 - 3\cos\theta_A + \cos^3\theta_A}\right)^{1/3}; \quad r_R = \left(\frac{\sin^3\theta_R}{2 - 3\cos\theta_R + \cos^3\theta_R}\right)^{1/3} \quad (6)$$

All of the advancing, receding, thermodynamic, and dynamic contact angles on different surfaces are summarized in Table 1.

We emphasize that the present work focuses on the final equilibrium printing area, which is determined by the real contact angles bounded by the advancing and receding contact angles. The contact angle measured in the present work corresponds to a small Weber number, indicating that the contact angle evolution is governed by the surface tension rather than the inertia effect.[48] When the inertia effect dominates, the contact angle can be greater than the advancing value or less than the receding value, but this is not the consideration of the current work. The inertia-dominated impact process only appears in the initial stage (nanoseconds to submiliseconds) of the droplet−substrate interaction, while at the late stage, the printed droplets tend to become stable, and the inertia effect becomes less profound. Impact velocities in case of inkjet printing is typically in the range of 3−15 m/s.[49] Wijshoff et al.[50] stated that the time scale of the impact phase for a droplet with a diameter of 20 μm is in the order of microseconds. After the impact phase, the droplet recoils back to its equilibrium shape, determined by the surface energies of the ink and substrates. Hu et al.[17] have also mentioned that the drop impact velocities typically range from 4 to 12 m/s, and they observed no significant difference in drop shape after 0.5 ms.

In our work, we specifically examine the quasistatic state of the printed droplets, where tiny droplets with a diameter of 20 mm merge to form a larger drop. This large drop tends toward the equilibrium state, so that the inertia effect can be neglected. The dispensing method for measuring the dynamic contact angle in this work is to mimic the late-stage movement of the printed droplets. However, measuring the exact contact angle with the volume used in inkjet printing (typically 10 pL) is comparatively difficult. Moreover, a low volume leads to a very fast evaporation behavior, which gives rise to a very small window for capturing high-quality images and videos during the evaporation process. Although the volume in the contact angle measurement system is different from that used in inkjet printing, the measured values for the advancing and receding contact angles are expected to be valid for both large and small volumes.

It should be noted that the hydrophobic ITO surface is relatively smooth, and we are able to find a saturated contact angle of the droplet on the ITO surface, as shown in Figure 2c,d. This unique value of the contact angle is related to the dynamic printing process, so we adopt this value as the input contact angle on ITO surfaces in the simulations. In contrast, the ablated glass is relatively rough. After the dynamic printing process, the contact angle can be any value between the advancing and receding contact angles, and it is challenging to find a unique contact angle to characterize the wettability. In this case, we use the so-called thermodynamic contact angle, which reveals the intrinsic wettability of the rough surface.

Printing Semiconductor Ink on Patterned Substrates. The indium nitrate precursor-based ink is printed on a patterned layout, as shown in Figure 1a for different drop volumes. The printing is performed in the horizontal *X*-direction. For instance, in order to print a final drop with a total volume of 100 pL, two layers are applied, each comprising 5 droplets, and the drop spacing is set at 10 μm along the printing direction (left to right). Likewise, to produce a film with a total volume of 200 pL, two layers are printed, with each layer consisting of 10 droplets. The final shape of the drop is strongly dependent upon the wetting of the ink on both the ITO and glass substrate. Figure 3 shows the optical micrograph of top views of the printed films for different volumes on

https://doi.org/10.1021/acs.langmuir.3c03297
Langmuir XXXX, XXX, XXX−XXX

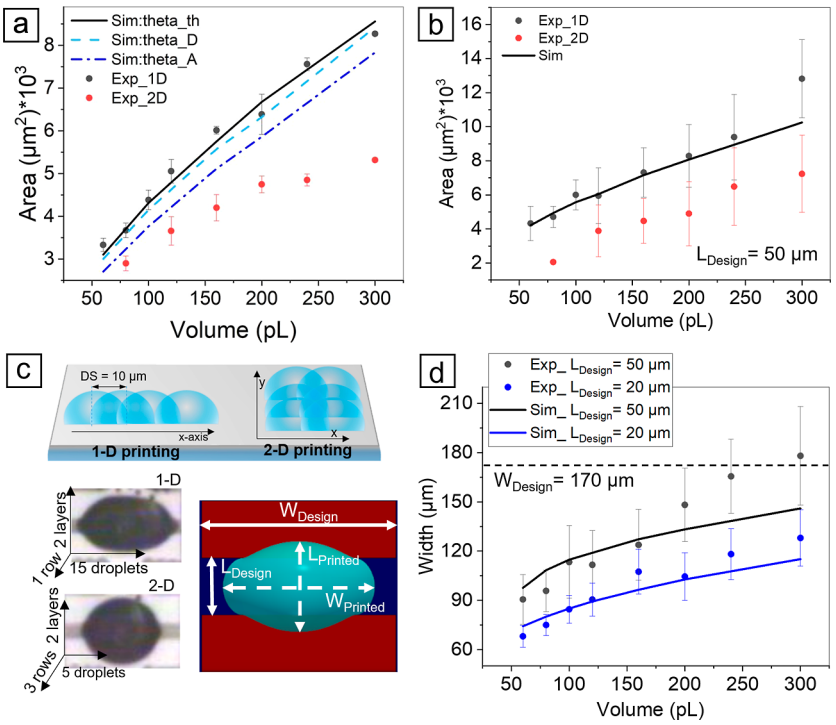

Figure 4. Area vs volume for the printed indium nitrate film on the ITO-patterned surfaces. (a) L_{design} = 20 μm and (b) L_{design} = 50 μm. Black symbols represent the printed film area with one-dimensional (1-D) printing (only in *X*-direction), and red symbols represent the results with two-dimensional (2-D) printing process (both in *X* and *Y* directions). Solid (black), dashed (cyan), and dot dashed (blue) lines represent simulation results considering θ_{th}, θ_D, and θ_A of ablated glass, respectively. (c) Top: scheme representing 1-D and 2-D printing. Bottom left: top view of printed drop with total volume of 300 pL for 1-D and 2-D printing strategy. 1-D: droplets are printed in one row with 15 droplets; 2-D: droplets are printed in three rows with each row containing five droplets. To print a total volume of 300 pL, two layers of droplets are printed for both 1-D and 2-D printing. Bottom right: scheme representing different geometric parameters of the printed film and pattern. (d) Subsequent width vs volume for different patterns with L_{design} = 50 μm (in black), and L_{design} = 20 μm (in blue). Error bar represents one standard deviation (n = 9). Solid lines correspond to simulation results.

ablated glass surface (Figure 3a) and on pattern substrates with channel lengths of 20 and 50 μm (Figure 3b).

For electronic devices, the current densities depend upon the channel length and width. Typical transfer characteristic of the field effect transistor follows $I_{ds} = (W/L)\alpha(V_{gs} - V_{th})^2$, where I_{ds}, V_{gs}, and V_{th} are drain current, gate voltage, and threshold voltage, respectively. The parameter α denotes other information such as capacitance and ion mobility. Drain current is directly proportional to channel width and inversely proportional to channel length. The proof of this equation for electrolyte gated transistors is presented in ref 34. We can also conclude from this equation that the channel width should be larger than the channel length for higher drain currents. Keeping this point in mind, we select design width around 170 μm and design length between 20 and 100 μm. Different volumes (V = 100, 200, and 300 pL) are considered. The corresponding simulation results are shown next to the experiments, where good agreement of the drop shapes and wetting areas are observed. Note that the printed drop is not circular on ablated glass but elliptical with a major axis along the printed direction. This is because of the pinning effect of the rough glass surface achieved by laser ablation of the ITO-coated glass substrate. Experimental and simulation results for the channel length of 80 μm are presented in the Supporting Information (Figures S5 and S6).

To quantitatively compare the simulation results with the experimental results, the base areas of the printed drops are calculated and plotted against the total volume of the printed ink, as illustrated in Figure 4a for L_{design} = 20 μm and in Figure 4b for L_{design} = 50 μm. It is observed that for the same volume, the printing strategy is a very important factor in determining the final shape of the drop, i.e., printing in 1-D or 2-D. Here, 2-D printing means that more than one row is printed to achieve one final drop of a certain volume. In the top panel of Figure 4c, the scheme for 1-D and 2-D printing is presented. Optical images at the bottom display the difference between 1-D and 2-D printing strategies of the drop with the total volume 300 pL. For the 1-D strategy, 15 droplets are printed along the *X*-direction (also the printing direction), whereas for the 2-D strategy, 3 rows, each row with 5 droplets in *X*-direction, are printed. We observe that the base area in the case of 1-D printing (black dots) is larger than that of 2-D printing (red dots) for a constant volume, as shown in Figure 4a,b. In the case of 2-D printing, the contact area of the final drop is comparatively smaller because a larger portion of the ITO surface (hydrophobic surface) is covered by the drop. The influence of area portions of hydrophilic and hydrophobic areas wetted by the drop base to the equilibrium drop shape has been theoretically addressed in the ref 40. Here, our result can be considered as a qualitatively experimental confirmation of this work. The base areas calculated from simulated images are shown with black solid lines, which are consistent with the 1-D printing results via experiments. In the simulations, the contact angles on the hydrophilic and hydrophobic areas are set as 59.4° (thermodynamic contact angle θ_{th}) and 92.5° (dynamic contact angle θ_D), respectively. To show the

https://doi.org/10.1021/acs.langmuir.3c03297
Langmuir XXXX, XXX, XXX−XXX

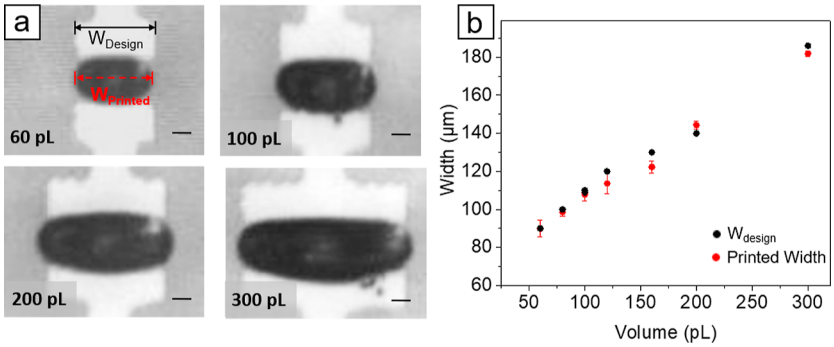

Figure 5. (a) Printed indium nitrate precursor film between the channels with varying widths (W_{design} = 80, 92, 120, and 186 μm) and fixed length (L_{design} = 50 μm). The printed volumes are selected from the plot in Figure 4d corresponding to each width. (b) Printed width (red symbols) plotted against the ink volume. Black symbols represent the designed widths W_{design} corresponding to each printed width. Scale bar: 20 μm.

influence of the dynamic contact angle on the ablated glass surface on the wetting morphology of the droplets, we choose two typical values of the dynamic contact angle (i.e., θ_D = 89 and 65°) on the ablated glass surface as input parameters in the simulations, while the contact angle on the ITO surface remains unchanged. The corresponding simulation results are depicted by the dashed and dotted dashed lines in Figure 4a. It is found that the contact area monotonically declines as the contact angle on the ablated glass changes from 59.4 to 65° and 89°. This result reveals that the rough nature of the ablated glass surface gives rise to a wide range of dynamic contact angle suffering from different equilibrium states of droplets. The complexity of this problem is that the dynamic contact angle on the glass does not converge to a specific value (Figure S4d). Once the inertial force is not important in comparison with capillary and viscous effects, the dynamic contact angle on the glass should be bound by the advancing and receding values. With the impact of the surface roughness, the equilibrium wetting states on glass are almost infinite. Suffice to say, any value between the advancing and receding contact angles is possible. Once the contact angle hysteresis is nonzero, this complex issue exists in the whole inkjet printing community, which is actually the motivation of the present discussion.

The difference in 1-D and 2-D printing in experiments is caused by the strong pinning effect on the glass surfaces (roughness = 30 nm). In the simulations, both the hydrophilic and the hydrophobic regions are ideally smooth, and thus only one unique equilibrium drop shape can be obtained for a certain volume. Differences in the printed shapes via the 1-D and 2-D printing strategy can be also observed in circularity measurements, as plotted in Figure S6 in the Supporting Information. For 1-D printing, the printed drops are more elliptical, whereas for 2-D printing, circularity increases as the number of printing rows increases. Important parameters for the electronic devices, such as the printed width and printed length of fabricated semiconductor film are extracted from the optical micrographs, since the design and channel lengths of the device are constant, and the channel width varies for different drop volumes. We show the printed width vs the printed volume for both L_{design} = 20 μm and L_{design} = 50 μm in Figure 4d. Overall, the experimental results are in good agreement with simulations, but it is obvious that the error bars become larger for larger volumes. The deviation between the experiments and simulations shows its dependence on the drop volume. When the drop volume is small, the previously merged drops on the glass surface tend to move toward the ITO surface. In this case, the real contact angle of the drop on the ITO surface approaches the advancing contact angle. As the drop volume increases, more area on the ITO surface is occupied by the printed drop, and the outward tendency of the contact line movements becomes less profound. In this case, the contact angle of the drop on the ITO surface can be any value that spans from the receding to advancing contact angles. This explains the larger error bars for the drop with larger volumes. However, in simulations, the contact angle on the ITO is set with the measured dynamic contact angle, which is overestimated for a large volume and underestimated for small volume regions. Note that for all the results discussed above, we keep the designed width of the pattern (170 μm) constant, as highlighted by the dashed line in Figure 4d. As the drop volume increases, the width of the printed drops gradually approaches the designed width of the pattern.

Next, we make use of the relation of the printed width and volume achieved so far to reduce the deviation of the design width to the printed width. In Figure 5, ITO glass-based patterns with different design widths and fixed design length (50 μm) are prepared. The printed volume corresponding to each width is extracted from the plot shown in Figure 4d (black dots). We directly printed the drops with the chosen volumes on the designed patterns without any additional test prints. Top views of the resultant printed drops for the volumes V = 60, 100, 200, and 300 pL are shown in Figure 5a. The corresponding printed widths (red dots) are plotted as a function of the drop volume. As a reference, the designed width values (black dots) are also shown. The deviations of the printed widths from the designed widths are convincingly small. This shows that the produced results for the relation between printed area, printed width, and printed length can be directly deployed to the automated printing software to print films of varying dimensions on rectangular patterned substrates.

Enhancement of Fabrication Quality by Surface Modification. When a large number of devices are printed, variations in the printed widths and printed lengths are frequently observed. This is due to inevitable deviations during the printing process such as printer offset in the micrometer scale. Other than optically controlling the printing position, one approach is to increase the interfacial energy differences between ITO and glass surfaces. In the current work, we chemically functionalize the ITO surface with salinization and thiol−ene processing to make it comparatively more hydrophobic. The variation of the hydrophobicity is demonstrated by changing θ_A from 100 to 115°, as shown in Table 1. This

https://doi.org/10.1021/acs.langmuir.3c03297
Langmuir XXXX, XXX, XXX−XXX

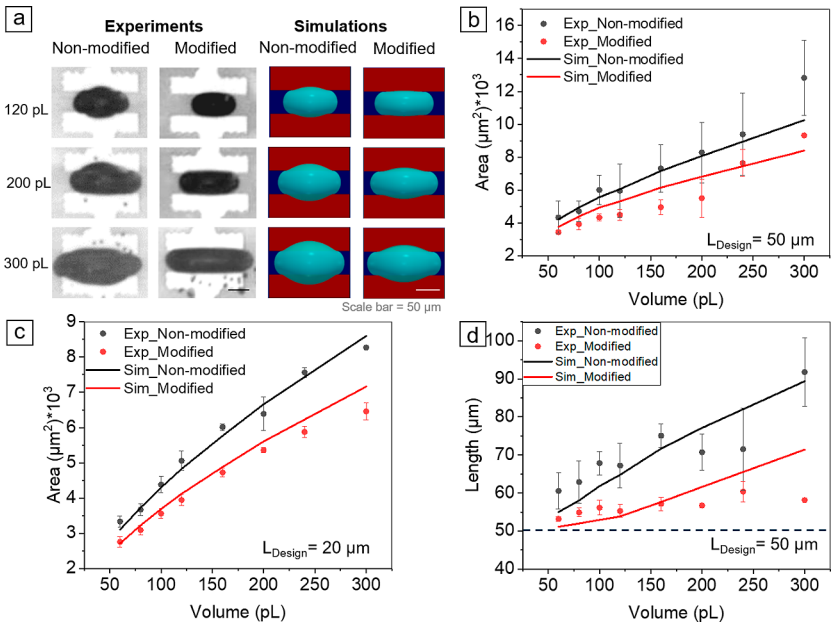

Figure 6. (a) Optical micrograph of inkjet-printed indium nitrate film between modified and nonmodified ITO-patterned substrates. Corresponding simulation figures are on the right side. (b) Area of the printed film on the patterned substrate with L_{design} = 50 μm plotted against different volume plotted for both modified (red symbols) and nonmodified substrates (black symbols). Solid lines represent the simulation data. Error bar represents 1 standard deviation (n = 9); (c) area vs volume for L_{design} = 20 μm for both modified and non-modified substrates. (d) For L_{design} = 50 μm, the printed length is plotted against volume for modified and nonmodified surfaces.

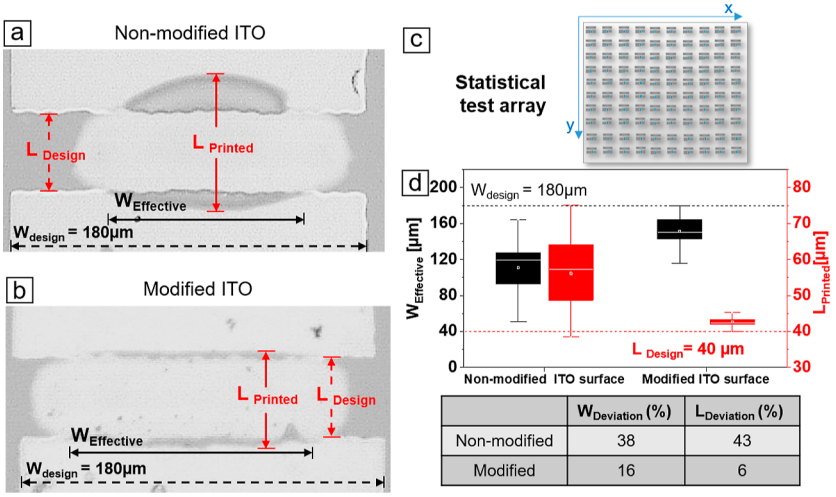

	$W_{Deviation}$ (%)	$L_{Deviation}$ (%)
Non-modified	38	43
Modified	16	6

Figure 7. Printed annealed (at 400 °C) In_2O_3 film between the channel of design length of 40 μm and design width of 180 μm. (a) On nonmodified ITO surfaces and (b) on the modified ITO surface. The effective widths of printed films are extracted for about 80 samples for each kind of surface, as shown in panels (a,b). (c) Statistical test arrays of the printing pattern. All 80 films are printed with only one command in the beginning. (d) Effective width (black box) and printed length (red box) are plotted for both modified and nonmodified ITO surfaces. Relative percentage deviations are shown in the table below. Both width and length variations are reduced in the case of a modified surface.

modification of the wettability helps in keeping the water-based semiconductor inks within the defined channel area (the glass surface bounded by the ITO patterns) even when the printing origin shifts a few micrometers up or down to the ITO surface. Therefore, the overall fabrication quality and robustness can be finely tuned and improved in the inkjet printing process. The difference in the printing shapes on the modified ITO and nonmodified ITO surface based pattern is shown in Figure 6. It is observed that for a constant volume, the spreading area of ink on nonmodified substrate is larger than that on the modified surface (Figure 6a). This is because the modified surface is relatively more hydrophobic as θ_A is increased to 115°, prohibiting the spreading of the ink.

We have also quantitatively shown that the total area of printed film on the modified surface (red dots) is lower than that on the nonmodified surface (black dots), as displayed in Figure 6b,c for the two design lengths 50 and 20 μm, respectively. Results from PF simulations are in good agreement with the experimental data and are represented by a solid line in Figure 6b,c. The printed lengths of the drops as a function of the droplet volume for modified and nonmodified substrates are shown in Figure 6d, where the design length of the pattern is fixed (50 μm). It is observed that the deviation of

https://doi.org/10.1021/acs.langmuir.3c03297
Langmuir XXXX, XXX, XXX−XXX

the printed length from the design length is comparatively lower for the modified ITO patterns (red dots) than that for the nonmodified ITO patterns (black dots), as shown in Figure 6d.

Our explanation for the statistical deviation between the simulations and experimental results is as follows. First, in the experiments, there is roughness on the real surfaces either on the ITO surfaces or on the ablated glass surface. The roughness gives rise to multiple possible metastable states of droplets due to the contact line pinning effect on the rough structure. Also, the glass surface is comparatively rougher than the ITO surface. The base area of the printed drop on ablated glass in the case of 50 μm channel length is larger than that on the ablated glass surface with 20 μm channel length. This results in more area deviation for the surface with 50 μm channel length, because there are more metastable states for a larger base area of the printed drop.[51] Second, we can reduce this variation by restricting the ink within the channel via increasing the surface energy differences between ITO and glass. From the plots in Figure 6b, we can interpret that the standard deviation of the printed length is significantly lower for modified ITO surfaces due to a stronger pinning effect at the boundary of two surfaces. Note that for all volumes, the printed length of the drop is greater than the design length L_{Design} of the pattern (horizontal dashed line in Figure 6d). It is highly required to ensure the good overlapping of the semiconductor film with the electrodes to achieve a low contact resistance. In the case of an even higher contact angle of the ITO surfaces, there is a possibility of weak contact between electrodes and the semiconductor layer, which will result in degraded electrical behavior of the electronic device. A reasonable contact area between the semiconductor film and the electrodes defines the compromise between sufficient overlapping and small variations for the dimensions of the printed films. The wettability contrast of the glass and ITO surfaces is proved to be the most crucial factor in this respect.

To compare the difference in fabrication yield on modified and nonmodified ITO patterned surface, we have printed 80 devices using a semiconductor precursor ink, as shown in Figure 7c. The design length and design width of the channel are chosen to be 40 and 180 μm, respectively. Printed volume and printed strategy are kept constant as 300 pL and $15 \times 1 \times 2$ ($X \times Y \times Z$), respectively. The printed length and effective channel width (corresponding to electronic devices) are calculated for all the printed films after annealing at 400 °C, as shown in Figure 7a,b. This annealing temperature is used as it is optimized for an indium oxide semiconductor film. However, FET devices can also be fabricated with a minimum sintering temperature of 280 °C, which provides the possibility to utilize indium nitrate based ink as a semiconductor material for FET fabrication on flexible substrates. Singaraju et al. presented their work utilizing similar indium nitrate ink on PET substrate.[10] Box plots representing the range and median of measured effective width and printed length for nonmodified and modified ITO surfaces are shown in Figure 7d. The percentage of the deviation for the effective width and printed length to design width and design length, respectively, are calculated as shown in the table shown in Figure 7. The results clearly indicate that the deviation of the printed width is reduced to half and printed length is reduced to 1/7 by surface modification of the ITO surface.

CONCLUSIONS

The wetting behavior and resulting printing dimensions of inkjet-printed indium nitrate precursor inks are examined for various patterned substrates. The shape (base area, printed length, and printed width) of the printed drop is investigated for different total volumes and for distinct layouts of the patterned substrates. PF simulations based on the free energy minimization are performed to confirm the wetting morphologies of the ink on the patterned and chemically modified substrates. Different types of contact angles on the ITO and glass surfaces are measured experimentally. Considering the DOD inkjet printing process and the rough nature of the real surface, suitable contact angles are chosen, which serve as the input parameters in the PF simulations. The overall good agreement between simulations and experimental results shows the justification of the digital twin based on PF simulations. It is shown that the printing strategies, such as 1-D printing and 2-D printing in experiments, affect the final shape of the ink owing to the pinning effect on the glass surfaces and the influence of the area portion of printed drops on hydrophobic (ITO) and hydrophilic (glass) areas.

Furthermore, the ITO surface is modified by chemical functionalization to increase the contact angle difference between the ITO and glass surfaces. In the case of the modified surface, the printed base area is more confined within the designed channel than that of the nonmodified surface. This result is also consistent with the work of Soltman et al.[52] who reported that an increase in the contact angle hysteresis allows for the printing of more precisely defined features. At last, we have presented the application of the modified surface for a large-scale printing fabrication with reduced variations in printed film dimensions. In the case of semiconductor printing, the percentage of deviation for the printed effective width and printed length with design width and design length is reduced to half and one-seventh, respectively, for the modified surface compared with the nonmodified surface. Our study provides essential guidelines for the highly precise printing technique widely applied in the fields of fabrication of integrated circuits, semiconductors, microchips, flexible and wearable electronics, sensors, and photovoltaic devices. Here, we verify our PF model for two experimental systems, which vary in their surface energy differences (modified ITO and nonmodified ITO). This model can also be extended to print rectangular films of other water-based inks in rectangular channels with other sets of two surface energies on any chemically patterned substrates.

A future direction deserving exploring is the investigation of the complex wetting behaviors for additional layers, such as printing electrolyte and PEDOT/PSS ink on the top of indium oxide film for complete fabrication of TFT. Specifically for electronic devices, it is very important to control the surface parameters (length, width, and thickness) to avoid device to device variations. Statistical comparison of electrical performance of completely fabricated transistors with normal ITO surface and modified ITO surface is presented in Supporting Information, Figure S7. The aim of this work is to reduce the device-to-device variation, which is strongly related to the surface morphologies of all the printed layers, as wettability on individual ink directly affects the interfaces between two materials, ink spreading, leakage currents, and cross connections between top layer to bottom layers. In particular, for gate material for our TFT, we chose PEDOT/PSS, which have

https://doi.org/10.1021/acs.langmuir.3c03297
Langmuir XXXX, XXX, XXX−XXX

proven its importance as a good conductive as well as organic semiconductor transparent film; therefore, its adhesion properties have also been studied heavily for different deposition techniques like spin coating and inkjet printing.[53−55] Similarly, for our transistors, it is vital to control the spread of gate material (PEDOT/PSS) ink over other electrodes and indium oxide film to avoid any leakage currents and short connections. Moreover, it warrants an in depth investigation on the dynamic evolution of the multicomponents in the ink and on the substrate, which should be coupled with evaporation and solidification effect.

■ ASSOCIATED CONTENT

Supporting Information

The Supporting Information is available free of charge at https://pubs.acs.org/doi/10.1021/acs.langmuir.3c03297.

Numerical setup and validation of modeling parameters, the layout for EGT, SEM images, contact angle measurement, printed drop shape analysis, and electrical performance analysis (PDF)

Time-dependent video of inkjet deposited 300 pL drop (AVI)

Contact angle measurement (AVI)

Advancing and receding contact angle of In_2O_3 on ITO surface (MP4)

■ AUTHOR INFORMATION

Corresponding Authors

Pooja Arya − *Institute of Nanotechnology, Karlsruhe Institute of Technology, Karlsruhe 76133, Germany;* orcid.org/0000-0001-8905-2015; Email: pooja.arya@kit.edu

Fei Wang − *Institute of Nanotechnology, Karlsruhe Institute of Technology, Karlsruhe 76133, Germany; Institute for Applied Materials−Microstructure Modeling and Simulation, Karlsruhe Institute of Technology, Karlsruhe 76131, Germany*; Email: fei.wang@kit.edu

Authors

Yanchen Wu − *Institute of Nanotechnology, Karlsruhe Institute of Technology, Karlsruhe 76133, Germany; Institute for Applied Materials−Microstructure Modeling and Simulation, Karlsruhe Institute of Technology, Karlsruhe 76131, Germany*

Zhenwu Wang − *Institute of Biological and Chemical Systems-Functional Molecular Systems, Karlsruhe Institute of Technology, Eggenstein-Leopoldshafen 76344, Germany; Institute of Organic Chemistry, Karlsruhe Institute of Technology, Karlsruhe 76131, Germany*

Gabriel Cadilha Marques − *Institute of Nanotechnology, Karlsruhe Institute of Technology, Karlsruhe 76133, Germany;* orcid.org/0000-0003-3718-7780

Pavel A. Levkin − *Institute of Biological and Chemical Systems-Functional Molecular Systems, Karlsruhe Institute of Technology, Eggenstein-Leopoldshafen 76344, Germany; Institute of Organic Chemistry, Karlsruhe Institute of Technology, Karlsruhe 76131, Germany*

Britta Nestler − *Institute of Nanotechnology, Karlsruhe Institute of Technology, Karlsruhe 76133, Germany; Institute for Applied Materials−Microstructure Modeling and Simulation, Karlsruhe Institute of Technology, Karlsruhe 76131, Germany; Institute of Digital Materials Science, Karlsruhe University of Applied Sciences, Karlsruhe 76133, Germany*

Jasmin Aghassi-Hagmann − *Institute of Nanotechnology, Karlsruhe Institute of Technology, Karlsruhe 76133, Germany;* orcid.org/0000-0003-0348-041X

Complete contact information is available at: https://pubs.acs.org/10.1021/acs.langmuir.3c03297

Author Contributions

#P.A. and Y.W. contributed equally to this work.

Notes

The authors declare no competing financial interest.

■ ACKNOWLEDGMENTS

This research is supported by VirtMat project "VirtMat P09: wetting Phenomena" of the Helmholtz association, as part of the programme "MSE-materials science and engineering" number-43.31.01. Authors G.C.M. and J.A.-H. acknowledge the financial support of the Deutsche Forschungsgemeinschaft (DFG, German Research Foundation) under Germany's Excellence Strategy via the Excellence Cluster "3D Matter Made to Order" (EXC-2082/1-390761711), which has also been supported by the Carl Zeiss Foundation through the "Carl-Zeiss-Foundation-Focus@HEiKA", by the State of Baden-Württemberg, and by the Karlsruhe Institute of Technology (KIT). Prof. P.L. and Z.W. thank DFG (Heisenberg professor project number: 406232485, LE 2936/9-1) for the financial support. Y.W. thanks Gottfried-Wilhelm Leibniz prize NE 822/31-1 of the German research foundation (DFG). The authors acknowledge support by the state of Baden-Württemberg through bwHPC.

■ REFERENCES

(1) Yang, L.; Rida, A.; Vyas, R.; Tentzeris, M. M. RFID Tag and RF Structures on a Paper Substrate Using Inkjet-Printing Technology. *IEEE Trans. Microwave Theory Tech.* **2007**, *55*, 2894−2901.

(2) Pranonsatit, S.; Worasawate, D.; Sritanavut, P. Affordable Ink-Jet Printed Antennas for RFID Applications. *IEEE Trans. Compon., Packag., Manuf. Technol.* **2012**, *2*, 878−883.

(3) Erozan, A. T.; Marques, G. C.; Golanbari, M. S.; Bishnoi, R.; Dehm, S.; Aghassi-Hagmann, J.; Tahoori, M. B. Inkjet-Printed EGFET-Based Physical Unclonable Function—Design, Evaluation, and Fabrication. *IEEE Trans. Very Large Scale Integr. (VLSI) Syst.* **2018**, *26*, 2935−2946.

(4) Marques, G. C.; Birla, A.; Arnal, A.; Dehm, S.; Ramon, E.; Tahoori, M. B.; Aghassi-Hagmann, J. Printed Logic Gates Based on Enhancement- and Depletion-Mode Electrolyte-Gated Transistors. *IEEE Trans. Electron Devices* **2020**, *67*, 3146−3151.

(5) Hu, H.; Scholz, A.; Singaraju, S. A.; Tang, Y.; Marques, G. C.; Aghassi-Hagmann, J. Inkjet-printed bipolar resistive switching device based on Ag/ZnO/Au structure. *Appl. Phys. Lett.* **2021**, *119*, 112103.

(6) Mishra, J. P.; Singh, K.; Chaudhary, H. *New Flexible Printed Circuit Electronic Devices and Their IoTs Applications*; Flexible Electronics for Electric Vehicles, 2023; pp 139−149.

(7) Adly, N.; Teshima, T. F.; Hassani, H.; Boustani, G. A.; Weiß, L. J.; Cheng, G.; Alexander, J.; Wolfrum, B. Printed Silk Microelectrode Arrays for Electrophysiological Recording and Controlled Drug Delivery. *Adv. Healthcare Mater.* **2023**, *12*, 2202869.

(8) Pinto, R. M. R.; Sankar Nemala, S.; Faraji, M.; Capasso, A.; Vinayakumar, K. B. Inkjet-Printing of Carbon Nano Onions for Sensor Applications in Flexible Printed Electronics. *2022 IEEE International Conference on Flexible and Printable Sensors and Systems*; Flexible and Printable Sensors and Systems, 2022; pp 1−4.

(9) Zhang, P.; Fu, Y.; Zhang, X.; Zhang, X.; Li, B.-W.; Nan, C.-W. Flexible high-performance microcapacitors enabled by all-printed two-dimensional nanosheets. *Sci. Bull.* **2022**, *67*, 2541−2549.
(10) Singaraju, S. A.; Marques, G. C.; Gruber, P.; Kruk, R.; Hahn, H.; Breitung, B.; Aghassi-Hagmann, J. Fully Printed Inverters using Metal-Oxide Semiconductor and Graphene Passives on Flexible Substrates. *Phys. Status Solidi RRL* **2020**, *14*, 2000252.
(11) Singh, M.; Haverinen, H. M.; Dhagat, P.; Jabbour, G. E. Inkjet printing—process and its applications. *Adv. Mater.* **2010**, *22*, 673−685.
(12) Wijshoff, H. The dynamics of the piezo inkjet printhead operation. *Phys. Rep.* **2010**, *491*, 77−177.
(13) Zhang, Y.; Hu, G.; Liu, Y.; Wang, J.; Yang, G.; Li, D. Suppression and Utilization of Satellite Droplets for Inkjet Printing: A Review. *Processes* **2022**, *10*, 932.
(14) Derby, B. Inkjet Printing of Functional and Structural Materials: Fluid Property Requirements, Feature Stability, and Resolution. *Annu. Rev. Mater. Res.* **2010**, *40*, 395−414.
(15) Wijshoff, H. Drop dynamics in the inkjet printing process. *Curr. Opin. Colloid Interface Sci.* **2018**, *36*, 20−27.
(16) He, B.; Yang, S.; Qin, Z.; Wen, B.; Zhang, C. The roles of wettability and surface tension in droplet formation during inkjet printing. *Sci. Rep.* **2017**, *7*, 11841.
(17) Hu, S.; Zhu, W.; Yang, W.; Li, M. Morphology simulation of drop-on-demand inkjet-printed. *npj Flexible Electron.* **2022**, *6*, 64.
(18) Soltman, D.; Smith, B.; Kang, H.; Morris, S. J. S.; Subramanian, V. Methodology for Inkjet Printing of Partially Wetting Films. *Langmuir* **2010**, *26*, 15686−15693.
(19) Seemann, R.; Brinkmann, M.; Kramer, E. J.; Lange, F. F.; Lipowsky, R. Wetting morphologies at microstructured surfaces. *Proc. Natl. Acad. Sci. U.S.A.* **2005**, *102*, 1848−1852.
(20) Matsui, H.; Noda, Y.; Hasegawa, T. Hybrid energy-minimization simulation of equilibrium droplet shapes on hydrophilic/hydrophobic patterned surfaces. *Langmuir* **2012**, *28*, 15450−15453.
(21) Zheng, Z.; Azzaroni, O.; Zhou, F.; Huck, W. T. S. Topography Printing to Locally Control Wettability. *J. Am. Chem. Soc.* **2006**, *128*, 7730−7731.
(22) Benor, A.; Hoppe, A.; Wagner, V.; Knipp, D. Microcontact printing and selective surface dewetting for large area electronic applications. *Thin Solid Films* **2007**, *515*, 7679−7682.
(23) Lee, C.; Kang, B. J.; Oh, J. H. High-resolution conductive patterns fabricated by inkjet printing and spin coating on wettability-controlled surfaces. *Thin Solid Films* **2016**, *616*, 238−246.
(24) Sung, J.; Kang, B. J.; Oh, J. H. Fabrication of high-resolution conductive lines by combining inkjet printing with soft lithography. *Microelectron. Eng.* **2013**, *110*, 219−223.
(25) Nishimoto, S.; Kubo, A.; Nohara, K.; Zhang, X.; Taneichi, N.; Okui, T.; Liu, Z.; Nakata, K.; Sakai, H.; Murakami, T.; Abe, M.; Komine, T.; Fujishima, A. TiO2-based superhydrophobic−superhydrophilic patterns: Fabrication via an ink-jet technique and application in offset printing. *Appl. Surf. Sci.* **2009**, *255*, 6221−6225.
(26) Park, S. K.; Kim, Y.-H.; Han, J.-I. High-resolution patterned nanoparticulate Ag electrodes toward all printed organic thin film transistors. *Org. Electron.* **2009**, *10*, 1102−1108.
(27) Gao, L.; McCarthy, T. J. Contact angle hysteresis explained. *Langmuir* **2006**, *22*, 6234−6237.
(28) Kusumaatmaja, H.; Yeomans, J. Modeling contact angle hysteresis on chemically patterned and superhydrophobic surfaces. *Langmuir* **2007**, *23*, 6019−6032.
(29) Eral, H.; t Mannetje, D.; Oh, J. M. Contact angle hysteresis: a review of fundamentals and applications. *Colloid Polym. Sci.* **2013**, *291*, 247−260.
(30) Honisch, C.; Lin, T.-S.; Heuer, A.; Thiele, U.; Gurevich, S. V. Instabilities of Layers of Deposited Molecules on Chemically Stripe Patterned Substrates: Ridges versus Drops. *Langmuir* **2015**, *31*, 10618−10631.
(31) Wang, F.; Wu, Y.; Nestler, B. Wetting Effect on Patterned Substrate. *Adv. Mater.* **2023**, *35*, 2210745.
(32) Sowade, E.; Mitra, K. Y.; Ramon, E.; Martinez-Domingo, C.; Villani, F.; Loffredo, F.; Gomes, H. L.; Baumann, R. R. Up-scaling of the manufacturing of all-inkjet-printed organic thin-film transistors: Device performance and manufacturing yield of transistor arrays. *Org. Electron.* **2016**, *30*, 237−246.
(33) Cadilha Marques, G.; von Seggern, F.; Dehm, S.; Breitung, B.; Hahn, H.; Dasgupta, S.; Tahoori, M. B.; Aghassi-Hagmann, J. Influence of Humidity on the Performance of Composite Polymer Electrolyte-Gated Field-Effect Transistors and Circuits. *IEEE Trans. Electron Devices* **2019**, *66*, 2202−2207.
(34) Cadilha Marques, G.; Weller, D.; Erozan, A. T.; Feng, X.; Tahoori, M.; Aghassi-Hagmann, J. Progress Report on "From Printed Electrolyte-Gated Metal-Oxide Devices to Circuits". *Adv. Mater.* **2019**, *31*, 1806483.
(35) Wang, Z.; Cui, H.; Li, S.; Feng, X.; Aghassi-Hagmann, J.; Azizian, S.; Levkin, P. A. Facile Approach to Conductive Polymer Microelectrodes for Flexible Electronics. *ACS Appl. Mater. Interfaces* **2021**, *13*, 21661−21668.
(36) Nestler, B.; Wendler, F.; Selzer, M.; Stinner, B.; Garcke, H. Phase-field model for multiphase systems with preserved volume fractions. *Phys. Rev. E* **2008**, *78*, 011604.
(37) Hötzer, J.; Reiter, A.; Hierl, H.; Steinmetz, P.; Selzer, M.; Nestler, B. The parallel multi-physics phase-field framework Pace3D. *J. Comput. Sci.* **2018**, *26*, 1−12.
(38) Wu, Y.; Wang, F.; Selzer, M.; Nestler, B. Investigation of Equilibrium Droplet Shapes on Chemically Striped Patterned Surfaces Using Phase-Field Method. *Langmuir* **2019**, *35*, 8500−8516.
(39) Wu, Y.; Kuzina, M.; Wang, F.; Reischl, M.; Selzer, M.; Nestler, B.; Levkin, P. A. Equilibrium droplet shapes on chemically patterned surfaces: theoretical calculation, phase-field simulation, and experiments. *J. Colloid Interface Sci.* **2022**, *606*, 1077−1086.
(40) Wu, Y.; Wang, F.; Ma, S.; Selzer, M.; Nestler, B. How Do Chemical Patterns Affect Equilibrium Droplet Shapes? *Soft Matter* **2020**, *16*, 6115−6127.
(41) Steinbach, I. Phase-field models in materials science. *Modell. Simul. Mater. Sci. Eng.* **2009**, *17*, 073001.
(42) Jacqmin, D. Calculation of two-phase Navier−Stokes flows using phase-field modeling. *J. Comput. Phys.* **1999**, *155*, 96−127.
(43) Carlson, A.; Do-Quang, M.; Amberg, G. Modeling of dynamic wetting far from equilibrium. *Phys. Fluids* **2009**, *21*, 121701.
(44) Xu, X.; Wang, X. Derivation of the Wenzel and Cassie Equations from a Phase Field Model for Two Phase Flow on Rough Surface. *SIAM J. Appl. Math.* **2010**, *70*, 2929−2941.
(45) Korhonen, J. T.; Huhtamäki, T.; Ikkala, O.; Ras, R. H. A. Reliable Measurement of the Receding Contact Angle. *Langmuir* **2013**, *29*, 3858−3863.
(46) Tadmor, R. Line energy and the relation between advancing, receding, and young contact angles. *Langmuir* **2004**, *20*, 7659−7664.
(47) Chibowski, E.; Terpilowski, K. Surface free energy of sulfur—Revisited: I. Yellow and orange samples solidified against glass surface. *J. Colloid Interface Sci.* **2008**, *319*, 505−513.
(48) Schiaffino, S.; Sonin, A. A. Molten droplet deposition and solidification at low Weber numbers. *Phys. Fluids* **1997**, *9*, 3172−3187.
(49) van der Bos, A.; van der Meulen, M.-J.; Driessen, T.; van den Berg, M.; Reinten, H.; Wijshoff, H.; Versluis, M.; Lohse, D. Velocity profile inside piezoacoustic inkjet droplets in flight: comparison between experiment and numerical simulation. *Phys. Rev. Appl.* **2014**, *1*, 014004.
(50) Wijshoff, H. Drop dynamics in the inkjet printing process. *Curr. Opin. Colloid Interface Sci.* **2018**, *36*, 20−27.
(51) Wu, Y.; Wang, F.; Selzer, M.; Nestler, B. Droplets on chemically patterned surface: A local free-energy minima analysis. *Phys. Rev. E* **2019**, *100*, 041102.
(52) Soltman, D.; Smith, B.; Morris, S.; Subramanian, V. Inkjet printing of precisely defined features using contact-angle hysteresis. *J. Colloid Interface Sci.* **2013**, *400*, 135−139.

https://doi.org/10.1021/acs.langmuir.3c03297
Langmuir XXXX, XXX, XXX−XXX

(53) Wilson, P. *Morphology, Electrical and Electronic Properties of Inkjet Printed PEDOT: PSS*; University of Surrey: United Kingdom, 2012.
(54) Simaite, A.; Mesnilgrente, F.; Tondu, B.; Souères, P.; Bergaud, C. Towards inkjet printable conducting polymer artificial muscles. *Sens. Actuators, B* **2016**, *229*, 425−433.
(55) Singh, A.; Katiyar, M.; Garg, A. Understanding the formation of PEDOT: PSS films by ink-jet printing for organic solar cell applications. *RSC Adv.* **2015**, *5*, 78677−78685.

https://doi.org/10.1021/acs.langmuir.3c03297
Langmuir XXXX, XXX, XXX−XXX